Active control of simply supported cylindrical shells using the weighted sum of spatial gradients control metric

Pegah Aslani, Scott D. Sommerfeldt, and Jonathan D. Blotter

Citation: The Journal of the Acoustical Society of America **143**, 271 (2018);
View online: https://doi.org/10.1121/1.5020784
View Table of Contents: http://asa.scitation.org/toc/jas/143/1
Published by the Acoustical Society of America

Active control of simply supported cylindrical shells using the weighted sum of spatial gradients control metric

Pegah Aslani[a] and Scott D. Sommerfeldt
Department of Physics and Astronomy, Brigham Young University, Provo, Utah 84602, USA

Jonathan D. Blotter
Department of Mechanical Engineering, Brigham Young University, Provo, Utah 84602, USA

(Received 19 May 2017; revised 7 November 2017; accepted 22 December 2017; published online 19 January 2018)

It is often desired to reduce sound radiated from cylindrical shells. Active structural acoustic control (ASAC) provides a means of controlling the structural vibration in a manner to efficiently reduce the radiated sound. Previous work has often required a large number of error sensors to reduce the radiated sound power, and the control performance has been sensitive to the location of error sensors. The ultimate objective is to provide global sound power reduction using a minimal number of local error measurements, while also minimizing any dependence on error sensor locations. Recently, a control metric referred to as weighted sum of spatial gradients (WSSG) was developed for ASAC. Specific features associated with WSSG make this method robust under a variety of conditions. In this work, the WSSG control metric is extended to curved structures, specifically a simply supported cylindrical shell. It is shown that global attenuation of the radiated sound power is possible using only one local error measurement. It is shown that the WSSG control metric provides a solution approximating the optimal solution of attenuating the radiated sound power, with minimal dependence on the error sensor location. Numerical and experimental results are presented to demonstrate the effectiveness of the method.
 https://doi.org/10.1121/1.5020784

[KML] Pages: 271–280

I. INTRODUCTION

Cylindrical shells are one of the structures that are commonly used around us. It is often desirable to reduce the sound radiated from these vibrating structures. The method of controlling the vibration in such a way that it results in attenuation of the radiated sound power is known as active structural acoustic control (ASAC), first developed in the early 1990s. There has been a considerable amount of research done on ASAC for cylindrical shells.[1–6] Within this class of methods, the ultimate practical goal is to achieve attenuation of the global sound field using a minimal number of local error measurements. In addition to minimizing the number of error sensors needed, it would be desirable to minimize the dependence on error sensor location. The search for the method that satisfies these criteria and is optimally effective and practical has been ongoing.

In previous work, some methods have utilized an array of sensors for the error metric. In some cases, the number of sensors in the array can be quite large, thereby reducing the practicality of the method.[3,4,7] With these methods, sensitivity to placement of the error sensors can also be an issue. In the case of shaped piezoelectric patches, the practicality can be limited by the fact that the piezoelectric design is dependent on the structure's dynamic response and the modes that need to be controlled.[8–15] Regardless of the degree of practicality, the control results obtained were generally not optimal. Here, the term optimal is used to refer to the performance that results in the maximum attenuation of the radiated sound power.

In terms of achieving the optimal control, a number of methods have been investigated, including minimization of the kinetic energy, and the potential energy, as well as the radiated sound power.[1,2,16] While minimizing the sound power yields optimal control, it is not feasible in practice, since it requires the measurement and control of the sound power in real-time.

In 2012, Fisher and others presented the method of the "weighted sum of spatial gradients" (WSSG), which relies on only a few local measurements and resulted in the global attenuation of the power while providing minimal sensitivity to the error sensor location.[17] In Fisher's work, the error metric was referred to as "Vcomp." In subsequent work, this method was implemented on planar structures, and the error metric was referred to as WSSG.[18–21]

This paper presents the extension of the WSSG method to curved structures, and specifically applies the method to a simply supported cylindrical shell, with the objective of fulfilling the criteria mentioned above for practicality and convenience. For curved structures, the membrane and bending stresses are coupled, and this work investigated whether the WSSG method would still work effectively given this difference in the dynamic response. The WSSG control metric utilizes parameters that have some connection with the lowest order acoustic radiation modes. This similarity provides the ability to achieve attenuation of the radiated sound power using only one, or a few, local error measurements. The radiation modes for a cylindrical shell are noticeably different than for a flat plate, which also raised the question as to

[a]Electronic mail: Pegah.aslani@gmail.com

whether the WSSG method would be as effective as it is for flat structures.[22] The WSSG control metric also exhibits relatively little spatial variance which means that there is little dependence on the error sensor location, making the method rather robust. It is shown that the WSSG control metric is able to provide near optimal solutions, in comparison to methods that use global measurements.

In the remainder of this paper, the numerical model for the cylindrical shell is first described. The WSSG control metric is briefly overviewed, and numerical control results are presented. A comparison of the results obtained by minimizing the sound power, as well as by using the WSSG control metric and other previously studied control metrics is presented. In order to compare and evaluate the performance of the WSSG control, radiated sound power has been chosen as the quantifying metric. The radiated sound power has been calculated numerically using the radiation resistance matrix for the external radiation from cylindrical shells.[22] In order to estimate the radiated sound power experimentally, the ISO-3741 standard was used. It is shown that there is little dependence on the error sensor location. The numerical results are verified experimentally using a modified filtered-x LMS algorithm. Comparison of the numerical and the experimental results suggest that the overall trends between the numerical and the experimental results agree quite well.

II. METHODOLOGY

A. Development of WSSG for cylindrical shells

The WSSG control function consists of four spatial gradient terms, corresponding to a breathing mode, two rocking modes, and a twisting mode.[17] In order to construct the WSSG for the cylindrical shell geometry, consider a cylinder with length L and radius a, in cylindrical coordinates, where z denotes the dimension along the axis, and θ and r are the polar coordinates. The WSSG function can then be written for a cylindrical shell as

$$WSSG = \alpha w^2 + \beta \left(\frac{\partial w}{\partial z}\right)^2 + \delta \frac{1}{a^2}\left(\frac{\partial w}{\partial \theta}\right)^2 + \gamma \frac{1}{a^2}\left(\frac{\partial^2 w}{\partial z\, \partial \theta}\right)^2, \quad (1)$$

where w is the displacement in the radial direction and α, β, δ, and γ are the set of weights that when applied, yield a rather uniform field with little spatial variance. This is illustrated in Fig. 1, which shows the WSSG for a cylindrical shell driven at a frequency of 541 Hz, which corresponds to the (2,3) mode of this shell. It can be seen that there is little variation in the WSSG, except for a small region near the drive point.

For a single resonance frequency, it has been shown that by setting α to the arbitrary value of 1, each of the other weights will be inversely proportional to the square of the structural wavenumber of the corresponding resonance mode along the direction of the gradient.[17]

The squared form of the spatial gradients allows for a global optimal solution to exist. The spatial gradients can be measured using four closely spaced accelerometers as one integrated error sensor. Such a configuration is shown in Fig. 2.

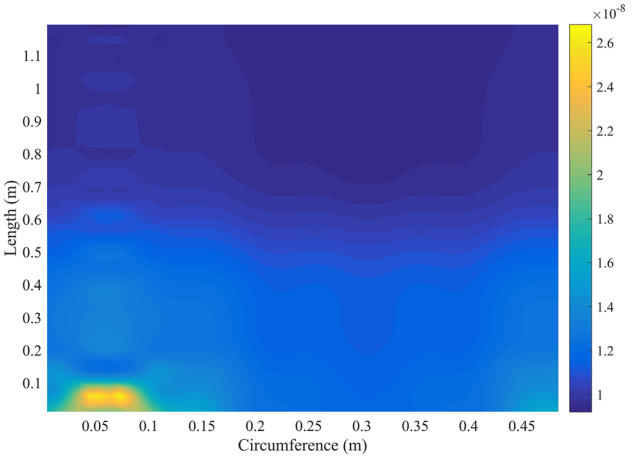

FIG. 1. (Color online) WSSG at frequency of 541 Hz for the (2,3) mode.

Using the finite difference method, the spatial gradients can be written as

$$\begin{aligned} w &= \frac{a_1 + a_2 + a_3 + a_4}{4}, \\ \frac{dw}{dz} &= \frac{a_1 - a_2 + a_3 - a_4}{2\Delta z}, \\ \frac{1}{a}\frac{dw}{d\theta} &= \frac{-a_1 - a_2 + a_3 + a_4}{2a\Delta\theta}, \\ \frac{1}{a}\frac{d^2w}{dz d\theta} &= \frac{-a_1 + a_2 + a_3 - a_4}{a\Delta z\Delta\theta}, \end{aligned} \quad (2)$$

where a_1, a_2, a_3, and a_4 are the signals from the four accelerometers, and Δz is the distance between a_1 and a_2, as well as between a_3 and a_4, along the axis of the cylinder. Also, $a\Delta\theta$ is the distance between a_1 and a_3, as well as a_2 and a_4, along the circumference. Since Eq. (2) is only the first term of the Taylor series expansion, it contains a truncation error on the order of (Δz^2), meaning that the larger the spacing between the sensors is, the larger the truncation error will be. There are also errors due to the random noise present in the signals from the sensors. Since some of the spatial gradient terms are obtained using subtraction of the accelerometer readings, if the accelerometers are spaced too closely and the noise floor is similar in magnitude to the magnitude of the difference between the two sensor

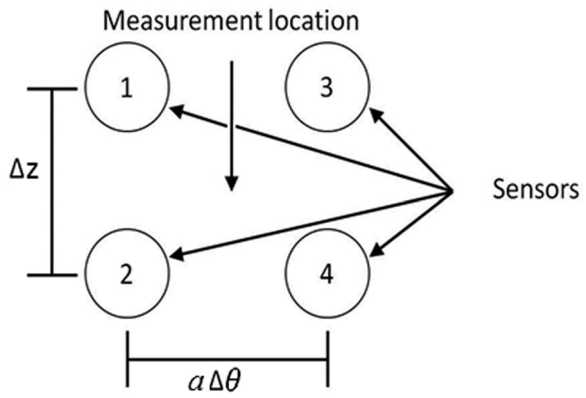

FIG. 2. The configuration of four closely spaced sensors.

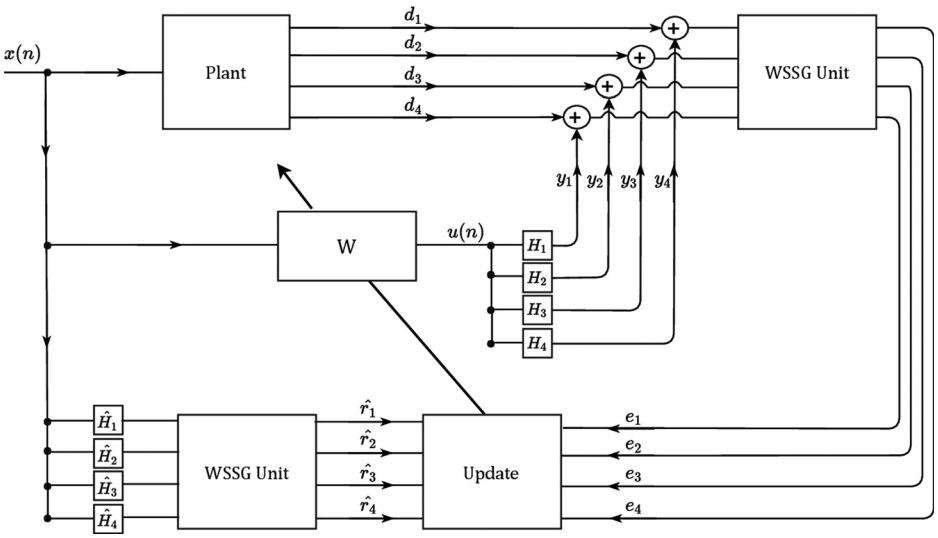

FIG. 3. Block diagram of the modified filtered-x LMS algorithm.

signals, the finite difference term will not be reliable. Thus, it is best to put the sensors farther apart to decrease this error. One can see that there is a tradeoff between spacing the accelerometers closer or farther apart. Hendricks has shown through an optimization process that the optimal distance for reducing these errors is about 1 in. (0.0254 m).[18]

B. Implementation of WSSG

Let **D** be the vector that contains the spatial gradient terms due to the primary force, with weighting applied. Similarly, the notation **G** will be used for the matrix which includes the spatial derivatives of the transfer function, g, between the secondary source(s) and the WSSG sensor with weighting applied. Equations (3) and (4) describe **D** and **G** as

$$\boldsymbol{D}^{\boldsymbol{T}} = \left[\sqrt{\alpha}\,w,\ \sqrt{\beta}\frac{\partial w}{\partial z},\ \sqrt{\delta}\frac{1}{a}\frac{\partial w}{\partial \theta},\ \sqrt{\gamma}\frac{1}{a}\frac{\partial^2 w}{\partial z \partial \theta}\right], \tag{3}$$

$$\boldsymbol{G}^{\boldsymbol{T}} = \left[\sqrt{\alpha}\,g,\ \sqrt{\beta}\frac{\partial g}{\partial z},\ \sqrt{\delta}\frac{1}{a}\frac{\partial g}{\partial \theta},\ \sqrt{\gamma}\frac{1}{a}\frac{\partial^2 g}{\partial z \partial \theta}\right]. \tag{4}$$

One can view each of the weighted gradient terms as one of the error components in an error vector used in an active control implementation. In general, one can establish the error signal vector as

$$\boldsymbol{e} = \boldsymbol{D} + \boldsymbol{G}\boldsymbol{u}, \tag{5}$$

where **u** is the vector of complex control forces with dimensions of $N \times 1$, where N is the number of control forces applied, and contains both amplitude and phase information for the control forces. If there are M error terms, **D** will have dimensions of $M \times 1$, and **G** will have dimensions of $M \times N$. In this case, since four spatial gradients are utilized, $M = 4$.

It can be shown that the optimal solution to minimize the squared error vector in Eq. (5) can be obtained as

$$\boldsymbol{u}_{opt} = -[\boldsymbol{G}^{\boldsymbol{H}}\boldsymbol{G}]^{-1}\boldsymbol{G}^{\boldsymbol{H}}\boldsymbol{D}. \tag{6}$$

This form can be used to numerically minimize the WSSG control metric. However, in practice, a modified filtered-x LMS algorithm is used to implement the WSSG control adaptively in real time. For more extensive information on modifying the filtered-x LMS algorithm in this manner, the reader is referred to the paper by Sommerfeldt and Nashif in 1994.[23]

In order to apply the filtered-x LMS algorithm to the WSSG control metric, one needs to adjust the algorithm to incorporate the gradients of the WSSG control metric. Hence, the algorithm described in the following will be referred to as the modified filtered-x algorithm. A schematic of the block diagram of this algorithm is shown in Fig. 3.

In this application, the excitation signal from the generator is input to the control system as a reference signal. Considering the WSSG control metric, one can see that four transducers, such as accelerometers, are needed in order to obtain the spatial gradients. These accelerometers correspond to subscripts 1, 2, 3, and 4 in Fig. 3. During the control operation, the response of each accelerometer is composed of the plant response through the primary path, resulting in the disturbance signals d_1, d_2, d_3, and d_4, respectively, and the secondary path response, resulting in the control signals, y_1, y_2, y_3, and y_4. These signals physically add together, so that the response of each accelerometer corresponds to $d_i + y_i$, where $i = \{1, 2, 3, 4\}$. These four accelerometer signals are then processed according to Eq. (2) to yield the spatial gradients. This additional processing is denoted by "WSSG unit" in the block diagram. Therefore, the final error signals (after being processed by the WSSG unit) can be written as

$$\begin{aligned}
e_1 &= \sqrt{\alpha}\left[\frac{d_1+d_2+d_3+d_4}{4} + \boldsymbol{u}^{\boldsymbol{T}}\left[\frac{\boldsymbol{H_1}+\boldsymbol{H_2}+\boldsymbol{H_3}+\boldsymbol{H_4}}{4}\right]\right],\\
e_2 &= \sqrt{\beta}\left[\frac{d_1-d_2+d_3-d_4}{2\Delta z} + \boldsymbol{u}^{\boldsymbol{T}}\left[\frac{\boldsymbol{H_1}-\boldsymbol{H_2}+\boldsymbol{H_3}-\boldsymbol{H_4}}{2\Delta z}\right]\right],\\
e_3 &= \sqrt{\delta}\left[\frac{-d_1-d_2+d_3+d_4}{2a\Delta\theta} + \boldsymbol{u}^{\boldsymbol{T}}\left[\frac{-\boldsymbol{H_1}-\boldsymbol{H_2}+\boldsymbol{H_3}+\boldsymbol{H_4}}{2a\Delta\theta}\right]\right],\\
e_4 &= \sqrt{\gamma}\left[\frac{-d_1+d_2+d_3-d_4}{a\theta\Delta z} + \boldsymbol{u}^{\boldsymbol{T}}\left[\frac{-\boldsymbol{H_1}+\boldsymbol{H_2}+\boldsymbol{H_3}-\boldsymbol{H_4}}{a\Delta\theta\Delta z}\right]\right],
\end{aligned} \tag{7}$$

where $\boldsymbol{H_1}$, $\boldsymbol{H_2}$, $\boldsymbol{H_3}$, and $\boldsymbol{H_4}$, are the actual secondary path transfer functions between the control source and each of the accelerometers. In Fig. 3, $\hat{\boldsymbol{H}}_1$, $\hat{\boldsymbol{H}}_2$, $\hat{\boldsymbol{H}}_3$, and $\hat{\boldsymbol{H}}_4$ are the estimates of these secondary path responses determined by an off-line system identification process (SysID) prior to control operation. In addition, $\hat{\boldsymbol{r}}_1$, $\hat{\boldsymbol{r}}_2$, $\hat{\boldsymbol{r}}_3$, and $\hat{\boldsymbol{r}}_4$ are the reference signal filtered by the estimates of the secondary path responses, $\hat{\boldsymbol{H}}_1$, $\hat{\boldsymbol{H}}_2$, $\hat{\boldsymbol{H}}_3$, and $\hat{\boldsymbol{H}}_4$, respectively, and then processed by the WSSG unit.

With this control structure in place, the control filter is then adaptively updated as

$$\mathbf{W}(t+1) = \mathbf{W}(\mathrm{t}) - \mu \sum_{i=1}^{4} e_i(t)\boldsymbol{R_i}(t), \tag{8}$$

where μ is the convergence factor, and $\boldsymbol{R_i}(t)$ is the vector of the current and past values of $\hat{\boldsymbol{r}}_i$.

C. Quantifying the control performance

The radiated sound power is chosen as the metric to quantify the performance of the WSSG control. Radiation modes corresponding to external radiation from a cylindrical shell are used to calculate the radiated sound power numerically.[22] They are also used in monitoring the radiation mode amplitudes before and after control in order to better understand the mechanism of sound power reduction using the WSSG control metric. For experimental results, the ISO-3741 standard has been used to estimate the radiated sound power in a reverberation chamber using six microphones.

III. NUMERICAL RESULTS

There are a number of shell theories that have been developed. However, in a paper by Farshidianfar, it was shown that the Soedel theory provides better results when compared to other theories considered.[24] Hence, in this paper, Soedel's shell theory for a thin-walled, simply supported, cylindrical shell is used to model the response of the shell due to a point excitation.[25] The resulting normal component of displacement is incorporated into Eq. (1) to yield the WSSG function.

For this case, a simply supported aluminum cylindrical shell with length 1.206 m, radius 0.0778 m, and thickness 0.0016 m is considered. The cylinder model is discretized using 2500 elements, with 50 elements along the circumference and 50 elements along the axis of the cylinder.

This results in dimensions of each element being 0.024 m along the axis, and 0.01 m along the circumference. The highest frequency considered here is 900 Hz, which corresponds to an acoustic wavelength of 0.38 m. Since the dimensions of the elements considered are significantly less than the smallest acoustic wavelength, the same discretization can be used for all frequencies in the range of interest.

The natural frequencies of modes corresponding to displacement in the normal direction are calculated using Soedel shell theory and are listed in Table I, where n is the axial mode number and m is the circumferential mode number.

TABLE I. Natural frequencies of the cylindrical shell.

Frequency (Hz)	n	m
203.06	1	2
290.23	1	1
413.91	2	2
505.27	1	3
540.71	2	3
653.77	3	3
814.28	3	2
866.07	4	3

As mentioned in Sec. II A, the WSSG weights for each resonance frequency are inversely proportional to the squared structural wavenumber in the direction of the corresponding gradient term. This corresponds to $\beta = (1/k_z)^2$, $\delta = (1/k_\theta)^2$, and $\gamma = (1/k_z\, k_\theta)^2$, where $k_z = (n\pi/L)$ and $k_\theta = (m/a)$. For instance, at 203.06 Hz the corresponding weights are $[1.0,\ 1.47 \times 10^{-1},\ 1.51 \times 10^{-3},\ 2.23 \times 10^{-4}]$. Applying a unique set of weights at each of the resonance frequencies, the WSSG field becomes very uniform, such that the spatial variance of the WSSG across the shell is less than 0.03%.

However, in order to apply WSSG control for all frequencies in the range of interest, it is desirable to use a single set of weights. Therefore, the weights are averaged over all the resonance peaks present in the frequency range of interest. In order to investigate the WSSG control metric, configurations **A**, **B**, **C**, **D**, and **E** were considered. The coordinates for these configurations are listed in Table II.

Figure 4 shows the results for the radiated sound power before and after WSSG control, where WSSG is minimized as a function of frequency.

In this figure, the solid line shows the radiated sound power before WSSG control and the dotted line shows the radiated sound power, after WSSG control. In addition, the radiated sound power can be numerically minimized with respect to the control force.[16] The dashed line represents the minimized radiated sound power, which determines the best possible attenuation that can be achieved for that particular source configuration. Here, the total sound power attenuation achieved using the WSSG control is 11.3 dB, while minimization of the radiated sound power predicts 13.7 dB attenuation.

Figure 5 shows the WSSG metric before and after control at the error sensor location. An overall attenuation of 17.7 dB is achieved. Note that the WSSG metric is a quantity

TABLE II. Locations of accelerometers (accel.) and actuators [$\boldsymbol{x}$ (m), θ (deg.)] for configurations (config.) **A**, **B**, **C**, **D**, and **E**.

	Config. **A**	Config. **B**	Config. **C**	Config. **D**	Config. **E**
Primary shaker	(0.1, 330)	(0.1, 330)	(0.2, 190)	(1.08, 10)	(0.1, 330)
Control shaker	(1.05, 150)	(1.05, 150)	(1.08, 10)	(0.20, 190)	(0.76, 102.5)
Accel. 1	(0.8, 282)	(0.69, 65)	(0.57, 320)	(0.57, 50)	(0.57, 228)
Accel. 2	(0.77, 282)	(0.66, 65)	(0.54, 320)	(0.54, 50)	(0.54, 228)
Accel. 3	(0.8, 302)	(0.69, 85)	(0.57, 340)	(0.57, 70)	(0.57, 248)
Accel. 4	(0.77, 302)	(0.66, 85)	(0.54, 340)	(0.54, 70)	(0.54, 248)

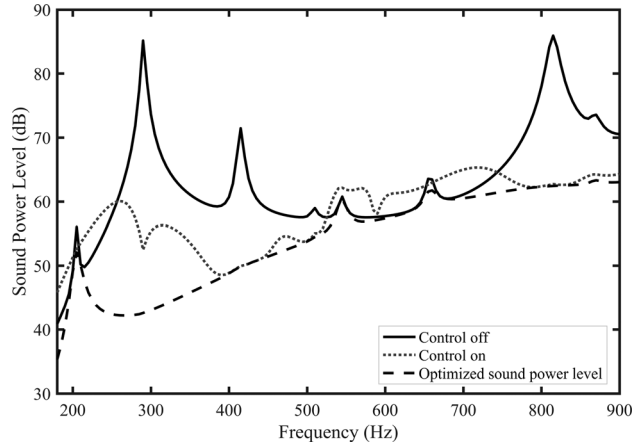

FIG. 4. WSSG control results predicted by the model for configuration **A**.

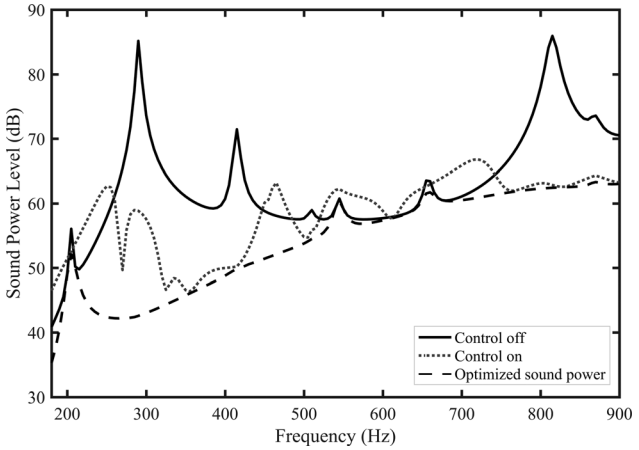

FIG. 6. WSSG control results predicted by the model for configuration **B**.

that depends only on the vibration of the structure and not on the acoustic radiation. However, it is a metric that has some correlation with the radiated sound power, so that attenuation of the WSSG metric generally results in attenuation of radiated sound power.

In order to investigate the dependence of the control performance on the sensor location, the sensors were moved to a different location in configuration **B**, while the actuators were kept in the same place. Since the WSSG is nearly uniform across the cylinder (see Fig. 1), changing the sensor location should have little effect on the overall performance. This test with configuration **B** was carried out to verify this assertion.

The WSSG control results for configuration **B** are shown in Fig. 6. In this case, the overall attenuation achieved using the WSSG control metric is 11.0 dB, resulting in less than 1 dB change in the overall attenuation by changing the sensor location.

Using the WSSG control, the overall attenuation for configurations **C**, **D**, and **E** is 10.8, 9.5, and −0.8 dB, respectively. It is useful to compare the performance of the WSSG control metric, using only one local measurement, with other methods that utilize global measurements in order to attenuate the radiated sound power.

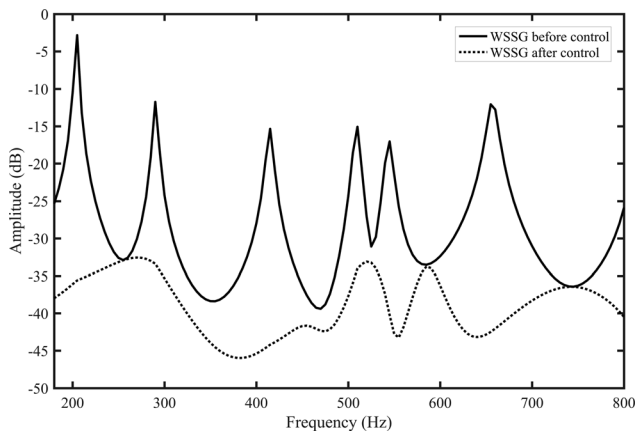

FIG. 5. WSSG metric before and after control at the error sensor location for configuration **A**.

Table III summarizes the performance of minimizing the radiated sound power, minimizing the WSSG control metric, minimizing the global kinetic energy, and minimizing the volume velocity for configuration **A**.

One can see that minimizing the radiated sound power offers the maximum amount of attenuation possible for this configuration, although it would require a significant number of point measurements resulting in a global measurement in order to achieve this result. Minimizing the global kinetic energy performs closely to minimizing the radiated sound power for this configuration, resulting in a slightly lower attenuation, but again requiring the use of a global measurement. Although volume velocity uses a global measurement as well, it actually enhances the overall radiated sound power. The WSSG control metric, using only one measurement location (with four accelerometers), results in 2.3 dB less attenuation than the optimal performance obtained by minimizing the radiated sound power. The results shown in Table III, as well as Figs. 4 and 6, indicate that the WSSG control metric is able to provide close to optimal performance for this shell using only one sensor location, while also exhibiting minimal dependence on the error sensor location. This suggests that this method can effectively substitute for any of the methods mentioned above in practice, with a robustness in error sensor positioning and an ease of implementation.

A. Acoustic radiation before and after control

In order to better understand the mechanism that results in sound power reduction, it is useful to compare the coupling between the vibration, before and after control, with the most efficient radiation modes at several resonances

TABLE III. Summary of performance of different methods for configuration **A**.

Method	Type of metric	Sound power level reduction
Minimizing sound power	Global	13.7 (dB)
Global kinetic energy	Global	12.1 (dB)
WSSG	Local	11.4 (dB)
Volume velocity cancellation	Global	−0.4 (dB)

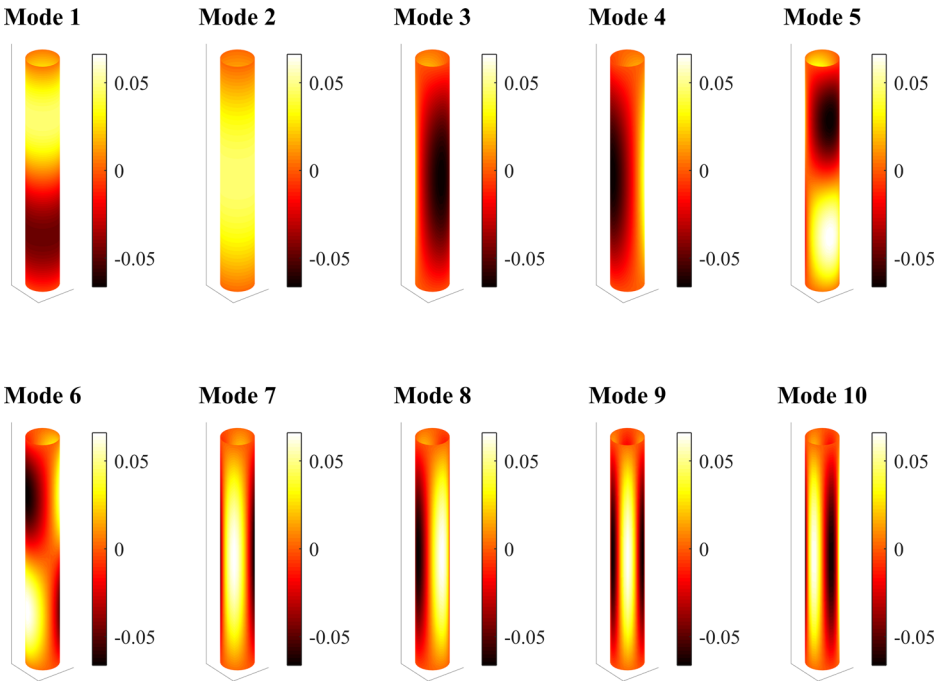

FIG. 7. (Color online) Ten most efficient radiation modes at 290.23 Hz, in order of efficiency.

where WSSG is able to attenuate the radiated sound considerably. For further discussion on radiation modes for cylindrical shells the reader is referred to Ref. 22. Figure 7 shows the ten most efficient radiation modes at a frequency of 290.23 Hz associated with the (1,1) structural mode. The corresponding eigenvalues, which are proportional to the modal efficiencies, are shown in Fig. 8.

Using the matrix of the eigenvectors for the radiation resistance matrix, i.e., $\boldsymbol{Q}$, and the structural velocity vector, $\boldsymbol{v}$, the radiation mode amplitudes, i.e., $s_i = \boldsymbol{Q}^T(:, i) \cdot \boldsymbol{v}$ for $i = 1, 2, \ldots, 10$, are calculated for the velocity fields before control (s_{bc}), after WSSG control (s_{ac}), and after minimizing the radiated sound power (s_{ac-opt}) in Table IV. As can be seen from the values listed in the table, the uncontrolled amplitude associated with radiation mode 4 (1.21) is the highest, followed by the radiation mode amplitude associated with radiation mode 3 (0.127), which has the next highest value. This can be understood by considering that the resonance at 290.23 Hz corresponds to the (1,1) mode, which most closely aligns with the velocity distribution of radiation modes 3 and 4, as can be seen in Fig. 7. Although the eigenvalues of radiation modes 3 and 4 are not the highest, the radiation mode amplitudes are sufficiently large to result in these modes dominating the resulting radiated sound power. The strong coupling rises from the fact that the high amplitude velocity field of the actual structure at its structural resonance closely matches the velocity distribution of those particular radiation modes. The radiation amplitude of mode 3 is lower due to the 90° shift of the velocity distribution in radiation mode 3. On the other hand, even though radiation modes 1 and 2 have the highest eigenvalues, i.e., they are more efficient than other modes at this frequency, since the velocity field of the vibration does not couple with them as strongly, they do not contribute greatly to the radiated sound power. Looking at the radiation amplitudes for higher order modes (for example, modes 7, 8, 9, and 10), we can see that the amplitudes are slightly higher than the amplitudes for the first two modes. The reason for this is that the velocity field of the structure is projected more effectively onto radiation modes that have the general trend of a $(1, m > 0)$ mode shape. Now looking at the values listed for s_{ac} (after WSSG control), for radiation mode amplitudes associated with radiation modes 3 and 4, the values drop to 9.1847×10^{-5} and 8.6961×10^{-4}, respectively, which leads to approximately 31 dB of sound power reduction. Comparing these values to the minimized power amplitudes, s_{ac-opt}, for modes 3 and 4, we can see that the values for WSSG control show similar trends to the optimal values listed under s_{ac-opt} for radiation modes 3 and 4. This suggests that there is a strong correlation between WSSG and the radiated sound power, since optimizing WSSG has led to similar results as for minimizing the radiated power.

IV. EXPERIMENTAL RESULTS

In order to verify the numerical results, a cylindrical shell with the properties mentioned in Sec. III was

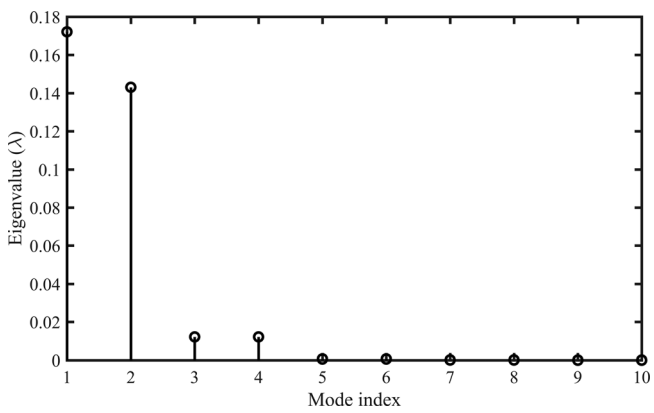

FIG. 8. Eigenvalues of the ten most efficient radiation modes at 290.23 Hz.

TABLE IV. Radiation mode amplitudes, before and after control, for the ten most efficient radiation modes at 290.23 Hz.

	s_{bc}	s_{ac}	s_{ac-opt}
Mode 1	-1.1676×10^{-3}	-7.0630×10^{-5}	-5.9740×10^{-5}
Mode 2	2.5131×10^{-3}	5.0015×10^{-3}	5.0262×10^{-3}
Mode 3	1.2722×10^{-1}	9.1847×10^{-5}	1.9270×10^{-7}
Mode 4	1.2104	8.6961×10^{-4}	1.8334×10^{-6}
Mode 5	-2.2861×10^{-3}	-4.4339×10^{-3}	-4.4552×10^{-3}
Mode 6	-1.1503×10^{-2}	-2.2310×10^{-2}	-2.2417×10^{-2}
Mode 7	1.7763×10^{-2}	3.5353×10^{-2}	3.5525×10^{-2}
Mode 8	-1.3518×10^{-2}	-2.6905×10^{-2}	-2.7036×10^{-2}
Mode 9	3.1516×10^{-2}	3.1177×10^{-4}	4.7739×10^{-8}
Mode 10	-1.0240×10^{-2}	-1.0130×10^{-4}	-1.5502×10^{-8}

fabricated. The simply supported boundary condition was approximated by machining a shallow groove at each end of the shell where a circular disk with a knife-edge was slightly press-fitted inside the groove. This was designed to give zero displacement but allow for a non-zero slope of the cylinder wall at the groove point.

As the next step in assembling the experimental set-up, it is important to mount the cylindrical shell in such a way that there is no distortion of the shell, nor any mass loading. In order to fulfill these requirements, the cylindrical shell was mounted vertically inside a frame. The framed cylinder was then placed in a reverberation chamber and hung from the ceiling, as well as lightly supported on a table stand to prevent unwanted rigid body motion. Vibration isolation materials were placed between the frame and the table stand in order to reduce vibration transmission to the table stand which could cause error in measurements of the radiated sound power. Four PCB model 352C68 accelerometers were mounted on the shell, according to Fig. 2, and two mini-shakers were attached to the shell as the primary and control sources.

To measure the radiated sound power, six microphones were used and spaced according to the ISO-3741standard. For this purpose, T_{60} measurements were made and meteorological conditions were monitored. A schematic of the complete setup is shown in Fig. 9.

The setup inside the control room included a PC that is connected to a Digital Signal Processing Board (DSP) utilizing a TI TMS320C6713GDP processor. For the results presented here, the control filter and the secondary path filter were both configured to have 20 coefficients. The DSP used the modified filtered-x algorithm to implement the active control. The setup also included a Brüel & Kjær (B&K) PULSE signal analyzer. An excitation output signal from one of the signal generators is directed into an amplifier and then into the primary, i.e., disturbance, shaker. In addition, the signal was input to the DSP, in order to provide the reference signal for the modified filtered-x LMS algorithm. The six microphones placed in the reverberation chamber were connected to the signal analyzer and used to obtain the measured sound power.

The accelerometers were connected to an ICP power supply. Using the outputs of the ICP power supply, the amplified accelerometers signals were then connected to an analog anti-aliasing filter. In addition, they were connected to the inputs of the B&K signal analyzer in order to be able to keep track of the accelerometer levels before and after control at each frequency. The output signals from the anti-aliasing filter were then input to the DSP, which implemented the ANC code to obtain the control signal. The accelerometer signals were processed to form the WSSG terms used to adaptively update the control filter. The output signal was conditioned using a reconstruction filter and amplifier, and then the signal was used to drive the control shaker.

Figure 10 shows the actual set up inside the reverberation chamber, showing the cylindrical shell installed in the frame while it is hung from the ceiling, with the shakers and the accelerometers attached. Figure 11 shows the microphone placing.

The cylindrical shell was scanned using a scanning laser Doppler vibrometer. In the frequency range below 700 Hz, resonance peaks observed in the FFT spectrum were at frequencies of 201.1, 310.6, 406.3, 510.1, 581.4, and 637.9 Hz.

The actual frequencies are somewhat different than those of the model, shown in Table I. The shift in the frequencies seems to be inconsistent. For example, the first frequency is lower than predicted in the model, but the second frequency is higher than predicted in the model. The

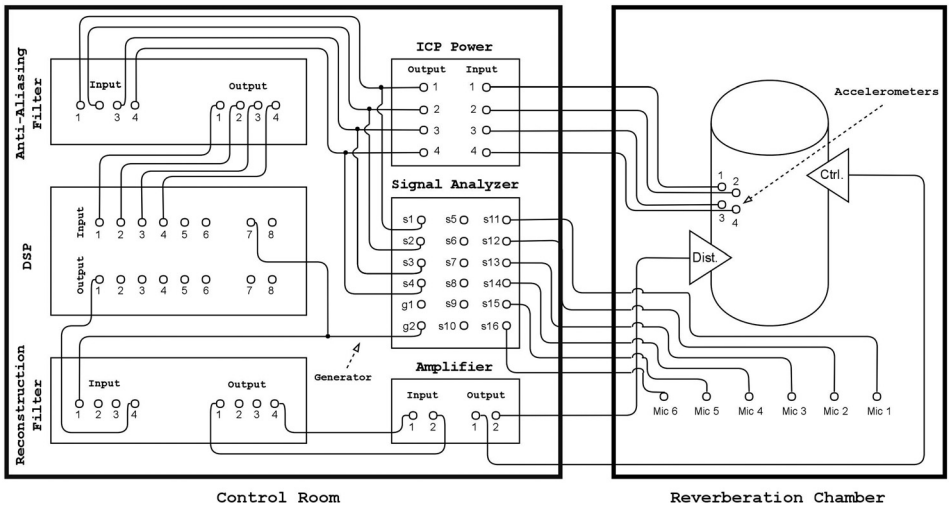

FIG. 9. Schematic of the complete experimental active control setup for the cylindrical shell.

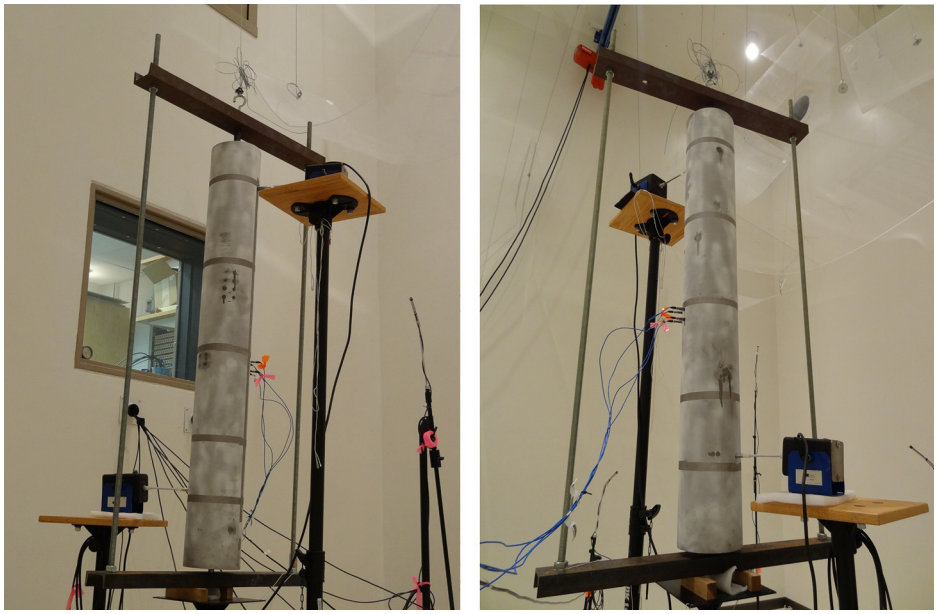

FIG. 10. (Color online) The experimental setup showing the mounted cylindrical shell in the frame while the accelerometers and shakers are attached.

discrepancies could be a result of slightly different values of dynamic parameters such as density, Young's modulus, etc., or that the cylinder is not completely behaving as an ideal simply supported cylindrical shell.

In order to achieve the best performance in sensing the WSSG terms, it is important to choose accelerometers with relatively close sensitivities. Therefore, the accelerometers were calibrated before each measurement and the relative sensitivities were inserted into the ANC code.

Once the SysID has been completed, the disturbance signal is activated and the sound pressure at each of the microphones is recorded due to only the disturbance signal, in order to determine the sound power with no control.

The WSSG control was implemented for the frequency range from 180 to 700 Hz, with frequency increments of 10 Hz. For this purpose, pressure data were recorded through the signal analyzer, where the bandwidth was limited to 1/24 octave bands with the center frequency matching that of the disturbance frequency. After recording the necessary data prior to control, the same set of data were measured while the ANC system was running. The pressure data were then processed to yield the radiated sound power.

The results of implementing the WSSG control experimentally for configuration **A** are shown in Fig. 12.

In this configuration, the overall sound power was attenuated by 5.7 dB. The damping factor in the model was adjusted to match the experimental damping factor; however, some differences might still be present. This can explain to some extent the difference between the experimental results and the model predictions. As can be seen in Fig. 12, the WSSG control metric is able to attenuate the radiated sound power effectively for all but one of the resonance peaks. It should also be noted that the Schroeder frequency of the chamber is about 300 Hz; therefore, the absolute value of the power measured below this frequency may not be completely accurate. However, this should not affect the change measured in the radiated power without and with control. Figure 13 shows the WSSG at the error sensor location before and after control, which is the metric

FIG. 11. (Color online) The experimental setup showing the cylindrical shell, shakers, and accelerometers, as well as the microphone placement.

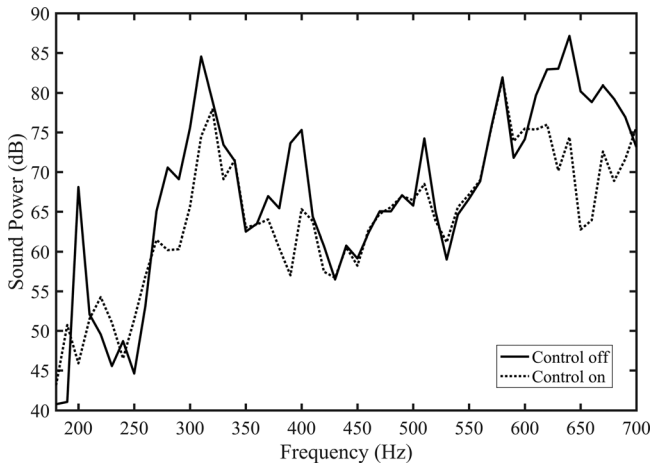

FIG. 12. Experimental WSSG control results for configuration **A**.

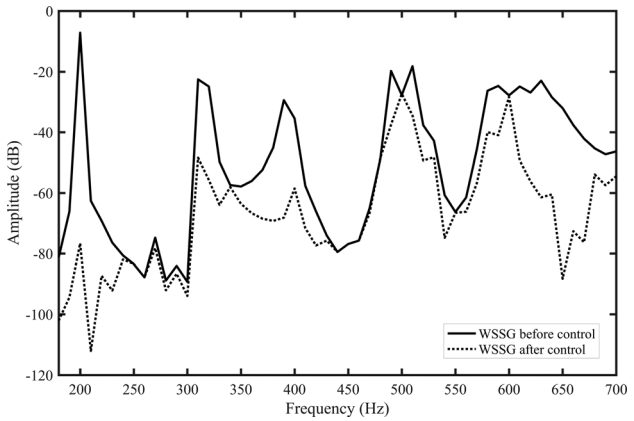

FIG. 13. Experimental WSSG before and after control.

actually minimized by the control system. For configuration **A**, 17.8 dB overall attenuation of WSSG was obtained.

Comparing Figs. 5 and 13, one can see that the results predicted by the model agree with the trends observed for the experimental results for the WSSG control metric. As can be seen, the attenuation of WSSG results in attenuation of the radiated sound power for most frequencies, which suggests that there is a correlation between the radiated sound power and WSSG.

In order to experimentally investigate the effect of sensor location on the control performance, the WSSG control metric was also implemented for configuration **B**. The control results for configuration **B** are shown in Fig. 14. In this case, the overall sound power attenuation is 4.9 dB.

In this configuration, the WSSG control metric is able to provide some attenuation for all resonance peaks.

Comparing this result with the experimental control result for configuration **A** in Fig. 12, one can see that there is only 0.8 dB difference in overall sound power attenuation. As was stated in Sec. III, there is usually only less than 1 dB variation when changing the error sensor location. Observing the performance of the WSSG control metric for different sensor locations verifies this result experimentally.

The WSSG control was investigated for configurations **C**, **D**, and **E**, as well. The overall attenuation for these configurations, as well as a summary of the overall attenuation of radiated sound power obtained both experimentally and numerically, are listed in Table V.

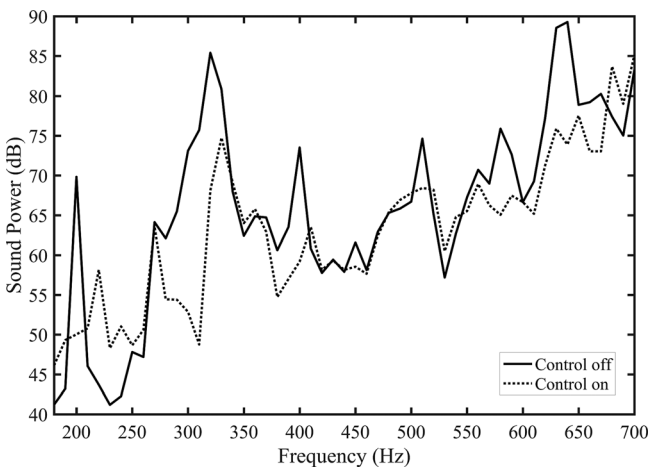

FIG. 14. Experimental WSSG control results for configuration **B**.

As can be seen from these results, the location for the control force in configurations **C** and **D** is less favorable in comparison with configurations **A** and **B**, in that less overall attenuation can be achieved in these cases. Although the performance of the WSSG control metric is only mildly dependent on the error sensor location, the location of the control force with respect to the disturbance force can be a more significant factor in determining the attenuation that can be achieved. For instance, configuration **E** presents a case where the location of the control force is knowingly chosen to be at a location which takes the least advantage of the circular symmetry of the cylindrical shell. In this case, due to the unfavorable location of the control force, the WSSG control metric has in fact enhanced the overall radiated sound power by 3.7 dB.

As can be seen from Table V, in general, the experimental results seem to follow the trends presented in the numerical results. As the control configuration is modified into less favorable locations, the control results in both the model and the experiment follow the same trend in yielding reduced sound power attenuation. The experimental results are also consistent for the case where the simulation results predict enhancement of radiated sound power, rather than attenuation.

V. CONCLUSIONS

The search for an ASAC method for cylindrical shells that provides the highest convenience and practicality, while providing optimal performance and robustness with respect to error sensor positioning, is still ongoing. The methods that result in an optimal control solution often employ global measurements, which generally makes these methods infeasible in practice. In this paper, the WSSG method was developed for simply supported cylindrical shells. The WSSG control metric was investigated numerically and the results suggest that this method can provide close to optimal solutions, while being robust with respect to the error sensor location. More importantly, this method is able to approximate the optimal sound power reduction for at least some configurations using only one point measurement.

The numerical model was investigated experimentally using a modified filtered-x LMS algorithm. The experimental dynamic analysis suggested that the cylindrical shell under study may not exhibit ideal simply supported boundary conditions. In spite of this, the experimental control

TABLE V. Summary of the model and experimental overall attenuation of radiated sound power for all configurations.

Configuration	Model	Experiment
Config. **A**	11.3 (dB)	5.7 (dB)
Config. **B**	11.0 (dB)	4.9 (dB)
Config. **C**	10.8 (dB)	4.5 (dB)
Config. **D**	9.50 (dB)	3.2 (dB)
Config. **E**	−0.83 (dB)	−3.7 (dB)

results suggest that the general trends agree well with the numerical results, and the WSSG control is able to control most of the resonance peaks similar to the numerical results. It is also shown that the general trends of the experimental results agree with the numerical results when the control source position is degraded. The effectiveness and robustness of this method, as well as the potential for a practical and convenient implementation, makes this method a suitable choice in applying ASAC on cylindrical shells.

ACKNOWLEDGMENTS

This research was supported by the National Science Foundation (Grant No. CMMI-1130482).

[1]D. R. Thomas, P. A. Nelson, and S. J. Elliott, "Active control of the transmission of sound through a thin cylindrical shell, part I: The minimization of vibrational energy," J. Sound. Vib. **167**, 91–111 (1993).
[2]D. R. Thomas, P. A. Nelson, and S. J. Elliott, "Active control of the transmission of sound through a thin cylindrical shell, part II: The minimization of acoustic potential energy," J. Sound. Vib. **167**, 113–128 (1993).
[3]K. Naghshineh, W. Chen, and G. H. Koopmann, "Use of acoustic basis functions for active control of sound power radiated from a cylindrical shell," J. Acoust. Soc. Am. **103**, 1897–1903 (1998).
[4]X. Pan and C. H. Hansen, "Active control of vibration transmission in a cylindrical shell," J. Sound. Vib. **203**, 409–434 (1997).
[5]C. R. Fuller, S. J. Elliott, and P. A. Nelson, *Active Control of Vibration* (Academic Press, San Diego, 1996), pp. 1–332.
[6]J. P. Maillard and C. R. Fuller, "Active control of sound radiation from cylinders with piezoelectric actuators and structural acoustic sensing," J. Sound. Vib. **222**, 363–387 (1999).
[7]A. Loghmani, M. Danesh, M. K. Kwak, and M. Keshmiri, "Active structural acoustic control of a smart cylindrical shell using a virtual microphone," Smart Mater. Struct. **25**, 1–12 (2016).
[8]S. D. Snyder and N. Tanaka, "On feedforward active control of sound and vibration using vibration error signals," J. Acoust. Soc. Am. **94**, 2181–2193 (1993).
[9]J. Qiu and J. Tani, "Vibration control of a cylindrical shell used in MRI equipment," Smart Mater. Struct. **4**, A75–A81 (1995).
[10]J. Tani, J. Qiu, and H. Miura, "Vibration control of a cylindrical shell using piezoelectric actuators," J. Intell. Mater. Syst. Struct. **6**, 380–388 (1995).
[11]V. Dogan and R. Vaicaitis, "Active control of nonlinear cylindrical shell vibrations under random excitation," J. Intell. Mater. Syst. Struct. **10**, 422–429 (1999).
[12]Y. Cao, H. Sun, F. An, and X. Li, "Active control of low-frequency sound radiation by cylindrical shell with piezoelectric stack force actuators," J. Sound. Vib. **331**, 2471–2484 (2012).
[13]H. S. Kim, J. W. Sohn, J. Jeon, and S.-B. Choi, "Reduction of the radiating sound of a submerged finite cylindrical shell structure by active vibration control," Sensors **13**, 2131–2147 (2013).
[14]J. W. Sohn and S.-B. Choi, "Active vibration control of a cylindrical structure using flexible piezoactuators: Experimental work in air and water environments," Smart Mater. Struct. **23**, 1–9 (2014).
[15]A. Loghmani, M. Danesh, M. Keshmiri, and M. M. Savadi, "Theoretical and experimental study of active vibration control of a cylindrical shell using piezoelectric disks," J. Low Freq. Noise Vib. Active Control **34**, 269–288 (2015).
[16]G. Jin, X. Liu, Z. Lio, and T. Yang, "Active control of structurally radiated sound from an elastic cylindrical shell," J. Marine Sci. Appl. **10**, 88–97 (2011).
[17]J. M. Fisher, J. D. Blotter, S. D. Sommerfeldt, and K. L. Gee, "Development of a pseudo-uniform structural quantity for use in active structural acoustic control of simply supported plates: An analytical comparison," J. Acoust. Soc. Am. **131**, 3833–3840 (2012).
[18]D. R. Hendricks, W. R. Johnson, S. D. Sommerfeldt, and J. D. Blotter, "Experimental active structural acoustic control of simply supported plates using a weighted sum of spatial gradients," J. Acoust. Soc. Am. **136**, 2598–2608 (2014).
[19]Y. Cao, S. D. Sommerfeldt, W. Johnson, J. D. Blotter, and P. Aslani, "An analysis of control using the weighted sum of spatial gradients in active structural acoustic control for flat panels," J. Acoust. Soc. Am. **138**, 2986–2997 (2015).
[20]W. R. Johnson, D. R. Hendricks, S. D. Sommerfeldt, and J. D. Blotter, "Active structural acoustic control of clamped flat plates using a weighted sum of spatial gradients," Shock Vib. **2015**, 628685 (2015).
[21]Y. Cao, S. D. Sommerfeldt, and J. D. Blotter, "Active structural acoustic control of plates with different boundary conditions using a weighted sum of spatial gradients," Proc. Inter-Noise **2015**, 3260–3270 (2015).
[22]P. Aslani, S. D. Sommerfeldt, and J. D. Blotter, "Analysis of the external radiation from circular cylindrical shells," J. Sound. Vib. **408**, 154–167 (2017).
[23]S. D. Sommerfeldt and P. J. Nashif, "An adaptive filtered-x algorithm for energy-based active control," J. Acoust. Soc. Am. **96**, 300–306 (1994).
[24]A. Farshidianfar and P. Oliazadeh, "Free vibration analysis of circular cylindrical shells: Comparison of different shell theories," Int. J. Mech. Appl. **2**, 74–80 (2012).
[25]W. Soedel, *Vibrations of Shells and Plates*, 3rd ed. (Marcel Dekker, New York, 2004), pp. 207–225.